

Lab on a Chip

Accepted Manuscript



This is an *Accepted Manuscript*, which has been through the Royal Society of Chemistry peer review process and has been accepted for publication.

Accepted Manuscripts are published online shortly after acceptance, before technical editing, formatting and proof reading. Using this free service, authors can make their results available to the community, in citable form, before we publish the edited article. We will replace this *Accepted Manuscript* with the edited and formatted *Advance Article* as soon as it is available.

You can find more information about *Accepted Manuscripts* in the [Information for Authors](#).

Please note that technical editing may introduce minor changes to the text and/or graphics, which may alter content. The journal's standard [Terms & Conditions](#) and the [Ethical guidelines](#) still apply. In no event shall the Royal Society of Chemistry be held responsible for any errors or omissions in this *Accepted Manuscript* or any consequences arising from the use of any information it contains.

ARTICLE

Induced-Charge Electroosmotic Trapping of Particles

Cite this: DOI: 10.1039/x0xx00000x

Yukun Ren,^{a,c,*} Weiyu Liu^{a,b,c} Yankai Jia,^a Ye Tao,^a Jinyou Shao^b, Yucheng Ding^b and Hongyuan Jiang^aReceived 00th January 2012,
Accepted 00th January 2012

DOI: 10.1039/x0xx00000x

www.rsc.org/

Position-controllable trapping of particles on the surface of a bipolar metal strip by induced-charge electroosmotic (ICEO) flow is presented herein. We demonstrate a nonlinear ICEO slip profile on the electrode surface accounting for stable particle trapping behaviors above the double-layer relaxation frequency, while no trapping occurs in DC limit as a result of a strong upward fluidic drag induced by a linear ICEO slip profile. By extending AC-flow field effect transistor from DC limit to AC field, we reveal that fixed-potential ICEO exceeding RC charging frequency can adjust the particle trapping position flexibly by generating controllable symmetry breaking in vortex flow pattern. Our results open up new opportunities to manipulate microscopic objects in modern microfluidic systems by using ICEO.

1. Introduction

Induced-charge electrokinetics (ICEK) describes a class of nonlinear electrokinetic effects sharing a unifying principle that an applied field acts on its own induced diffuse charge in a thin boundary layer on polarizable surfaces in contact with electrolytes [1-4], which has received considerable attention from the microfluidic community since the last decade. Recent advances on this subject include investigations into induced-charge electroosmotic (ICEO) flow around polarizable microstructures [5,6], induced-charge electrophoretic motion of freely suspended colloids [7-10], electro-rotation of metallic particles in a rotating electric field [11], and ICEK theory at large voltages [12, 13]. The basic slip mechanism at the solid/electrolyte interface in ICEK is named ICEO, and has quadratic dependence on the electric field intensity E due to a field-induced zeta potential $\zeta(E)$ [1]. Since it can persist in a low-frequency AC field with avoiding electrode reactions and bubble generation, ICEO flow serves as an important method for pumping and mixing in microfluidic lab-on-chip systems [3-5].

Despite to generate fast convective fluid flow around metal surfaces by ICEO sustained most interest, other promising applications on accurately moving, positioning, or trapping non-metallic particles using ICEO flow have been rarely tested, because of the unclear interplay between AC electric field, electrolyte ionic charge, fluid flow and particle motion [14]. To investigate this, we revisit the geometrical configuration of a floating bipolar electrode (Figure 1(a-d)) that has recently facilitated the validation of an improved standard model for ICEO [15]. Our motivation is to trap particles (yeast cells of finite downward buoyancy velocity as an example) at the flow stagnation region on the surface of the metal strip using ICEO vortex. Strong flow velocity and a linear slip profile on top of the inducing electrode are found below the double-layer relaxation frequency [15], which may be accompanied by a large upward ICEO flow component at the center (Figure 1(d)), resulting in a possible failure in particle trapping.

How to reduce the upward flow velocity thereby realizing reliable particle stagnation? A possible method is to lower the amplitude of applied voltage, which not merely reduces the upward flow component at the central region, but also damages ICEO flow velocity all around the inducing surface. Besides, raising the AC electric field frequency may be a feasible approach, since ICEO flow decays rapidly above a characteristic RC charging frequency due to a relaxation process thereby weakening the upward flow rates that may be counteracted by the downward buoyancy velocity. Adopting the latter, with increasing frequency beyond the reciprocal RC time scale, particle trapping behavior occurs on the electrode surface in our experiment. A nonlinear ICEO slip profile contributes to this successful trapping due to a spectrum of charging modes in the diffuse double layer. Under this circumstance, local ICEO fluid motion in the vicinity of the electrode edge is not severely affected by increasing frequency due to a higher relaxation frequency there, while small upward ICEO flow component induced by the extremely weakened ICEO slip at the central region realizes stable particle trapping. Furthermore, we are inspired by the concept of AC-flow field effect transistor (AC-FFET) to enable a flexible positioning of particle samples. By extending AC-FFET from DC limit to AC field, controllable formation of particle assembly line at desired locations is achieved by adjusting the gate potential of the bipolar metal strip. As compared to Eq.(5.5) in Ref.[3] obtained in a steady DC field, however, we find that fixed-potential ICEO above RC charging frequency is more effective in generating position-controllable flow stagnation region where stable particle trapping occurs.

2. Theoretical Basis

2.1 Quasi-electrostatics

Assuming electro-neutrality for the bulk electrolyte in the absence of magnetic effects, the set of Maxwell equations is formulated as:

$$\begin{cases} \rho_V = \nabla \cdot (\epsilon_f \mathbf{E}) \\ \frac{\partial \rho_V}{\partial t} + \nabla \cdot (\sigma_f \mathbf{E}) = 0 \\ \mathbf{E} = -\nabla \phi \end{cases} \quad (1)$$

Here \mathbf{E} is an imposed electric field, ϕ the bulk potential, ρ_V a volumetric free charge density existing only in the presence of dielectric gradients across the fluid bulk. ϵ_f and σ_f are the liquid permittivity and conductivity, respectively. Assuming homogeneous bulk salt concentration, Eq.(1) is further reduced to the Laplace equation:

$$\nabla^2 \phi = 0 \quad (2)$$

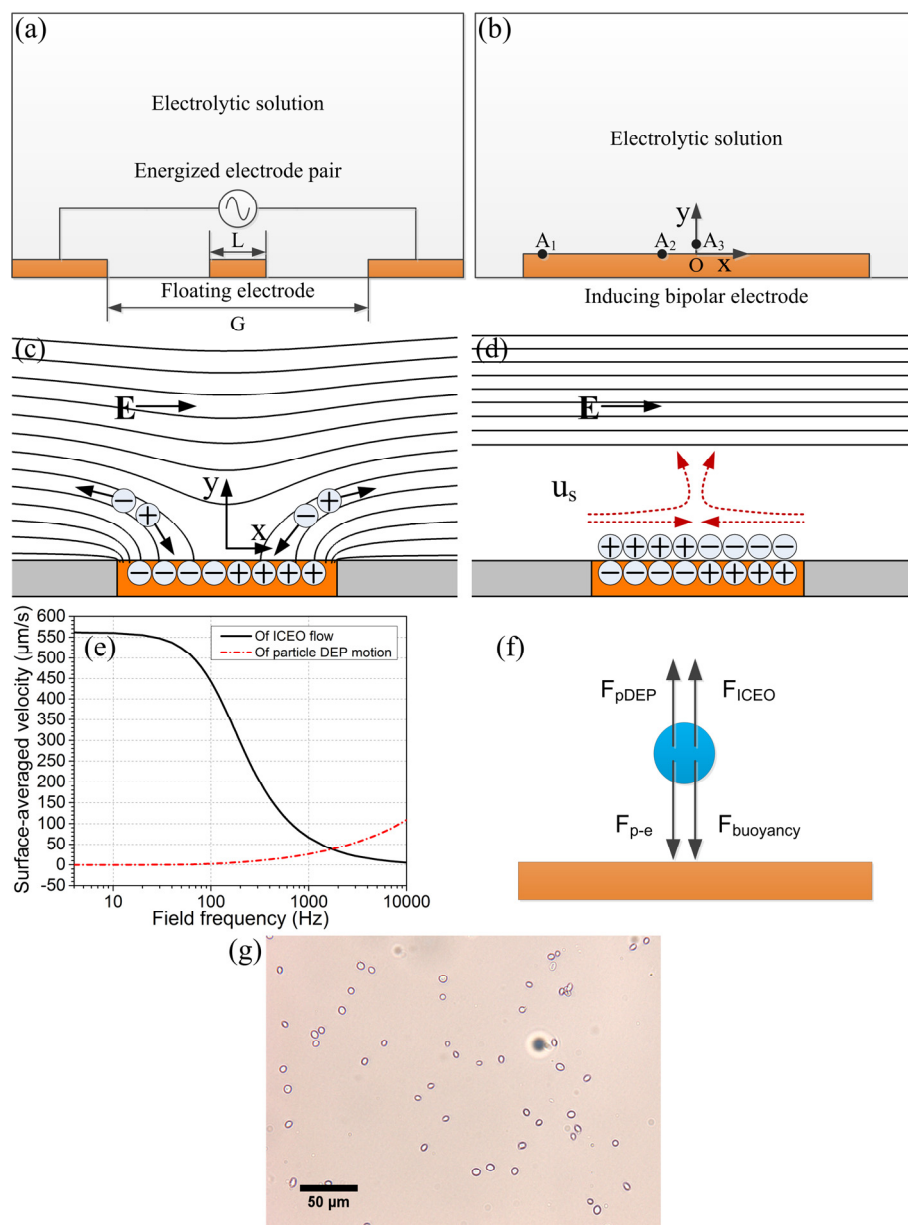


Figure 1 (a) Sketch of the device geometry used in our experiment: a middle electrode of $L=200\mu\text{m}$ in width is located at the center of the gap between an electrode pair separated by a distance of $G=3\text{mm}$. (b) Construction of 2-D x-y coordinate system with origin located at the center of the electrode surface, and positions of A1-A3 are chosen for velocity ratio calculations in Table 1. (c)-(d) Schematic diagram for basic physical process of ICEO around a floating metal strip (black lines and red dashed lines with arrow head denote the electric field lines and ICEO flow velocity vectors, respectively): (c) For a suddenly applied electric field, counter-ionic electro-migration to the bipolar electrode is initiated under the action of an original normal field component on the ideally polarizable surface; (d) After a characteristic RC charging time τ_{RC} , a dipolar diffuse screening cloud of a finite Debye length is formed at the metal/electrolyte interface due to the balance between electrostatic attraction and diffusion, leaving only tangential bulk field lines driving the ionic charge into ICEO streaming flow. (e) Frequency-dependent surface-averaged velocity of ICEO flow and particle DEP motion (for yeast cell) on top of the bipolar electrode. (f) An illustration of various forces acting on a particle just

above the center of the inducing electrode surface. (g) A micrograph of viable yeast cells under investigation activated by the method introduced in section 3.2.

2.2 Induced double-layer charging at the solid/electrolyte interface

For observable ICEO to occur, a conductive liquid media must be used, such that Ohmic current from the bulk resistance charges the diffuse screening cloud like a capacitor skin in the asymptotic limit of thin double layers:

$$\frac{\partial q}{\partial t} = \mathbf{n} \cdot \mathbf{J} = -\sigma_f (\mathbf{n} \cdot \nabla \phi) \quad (3)$$

Here $-q$ is the surface screening charge density in the induced double-layer (IDL), and \mathbf{n} an unit normal vector pointing from the electrode into the bulk. $\mathbf{n} \cdot \mathbf{J}$ represents the normal conduction current arriving at the outer rim of the Debye layer. For the diffuse layer, a linear charge-voltage relationship can be obtained:

$$q = C_d \zeta = C_d \frac{1}{1+\delta} (V_0 - \phi) \quad (4)$$

Here $\zeta = \phi_{OHP} - \phi = \frac{1}{1+\delta} (V_0 - \phi)$ is the induced zeta potential that contributes to induced electrokinetic flows, and $\delta = \frac{C_d}{C_s}$ denotes the surface physical capacitance ratio of the

diffuse layer $C_d = \frac{\epsilon_f}{\lambda_D}$ to the stern layer C_s . V_0 , ϕ_{OHP} and ϕ are the transient potential values at the metal surface, the outer Helmholtz plane between the two layers and in the bulk just outside IDL, respectively.

Substituting Eq.(4) into Eq.(3), we have:

$$\sigma_f (\mathbf{n} \cdot \nabla \phi) = \frac{C_d}{1+\delta} \frac{\partial (\phi - V_0)}{\partial t} \quad (5)$$

2.3 Interfacial ICEO slip

According to the Helmholtz-Smoluchowski formula for electroosmotic slip, the transient ICEO edge velocity on the polarizable surface can be derived:

$$\mathbf{u}_{slip} = -\frac{\epsilon_f \zeta \mathbf{E}_t}{\eta} = \frac{\epsilon_f}{\eta} \frac{1}{1+\delta} (\phi - V_0) (\mathbf{E} - \mathbf{E} \cdot \mathbf{n} \cdot \mathbf{n}) \quad (6)$$

Here $\eta = 0.001 Pa \cdot s$ is the dynamic viscosity of aqueous media, \mathbf{E}_t the tangential field component on the electrode surface.

Once the transient electric field and slip velocity are known, the Navier-Stokes equation for a low Reynolds number flow is solved to describe the progressive evolution of ICEO bulk fluid motion driven by the interfacial nonlinear electrokinetic slip:

$$\begin{cases} \rho \frac{\partial \mathbf{u}}{\partial t} = -\nabla p + \nabla \cdot (\eta (\nabla \mathbf{u} + (\nabla \mathbf{u})^T)) \\ \nabla \cdot \mathbf{u} = 0 \end{cases} \quad (7)$$

Here $\rho = 1000 kg/m^3$ is the liquid mass density, and p is hydraulic pressure.

2.4 Equations for sinusoidal steady state

As illustrated above, ICEO is transient in essence. Even in an AC field, the solid/electrolyte interface needs a finite time to response to the transient switching-on of the applied voltage due to electrochemical ion relaxation in the diffuse screening cloud. We concern sinusoidal steady state in practical experiments, however, so that phasor amplitude of each electric field variable as denoted by a tilde is hence introduced here for analytical convenience:

$$\phi(t) = A \cos(\omega t + \theta) = \text{Re}(A e^{j\theta} e^{j\omega t}) = \text{Re}(\tilde{\phi} e^{j\omega t}) \quad (8)$$

Here $\text{Re}(\dots)$ is the real part of (\dots) . A sinusoidal voltage signal in time domain $\phi(t) = A \cos(\omega t + \theta)$ corresponds to $\tilde{\phi} = A e^{j\theta}$ in phasor notation. On introducing phasor amplitude, all the equations above can be recasted to frequency domain by time-harmonic analysis.

Governing equation for the electric field is:

$$\nabla^2 \tilde{\phi} = 0 \quad (9)$$

On the ITO driving electrodes, we neglect double-layer polarization:

$$\tilde{\phi} = A_1 e^{j\theta} \text{ (left driving electrode) and } \tilde{\phi} = 0 \text{ (right)} \quad (10)$$

The RC charging condition on the middle electrode becomes:

$$\sigma_f (\mathbf{n} \cdot \nabla \tilde{\phi}) = j\omega \frac{C_d}{1+\delta} (\tilde{\phi} - \tilde{V}_0) \quad (11)$$

Here $\tilde{V}_0 = A_1 e^{j\theta} / 2$ is the floating potential of the bipolar metal strip, $C_0 = \frac{C_d}{1+\delta}$ the interfacial total capacitance. For fixed-potential ICEO, $\tilde{V}_0 = A_0 e^{j\theta}$.

Zero normal voltage flux on all insulating surfaces is:

$$\mathbf{n} \cdot \nabla \tilde{\phi} = 0 \quad (12)$$

Time-averaged ICEO slip velocity on polarizable surfaces under AC forcing can be derived from generalization of Helmholtz-Smoluchowski formula:

$$\begin{aligned} \langle \mathbf{u}_{slip} \rangle &= -\frac{\epsilon_f \langle \zeta \mathbf{E}_t \rangle}{\eta} = -\frac{\epsilon_f}{\eta} \frac{1}{2} \text{Re}(\tilde{\zeta} \tilde{\mathbf{E}}_t^*) \\ &= -\frac{\epsilon_f}{\eta} \frac{1}{2} \text{Re}\left(\frac{1}{1+\delta} (\tilde{V}_0 - \tilde{\phi}) \tilde{\mathbf{E}}_t^*\right) \\ &= \frac{1}{2} \frac{\epsilon_f}{\eta} \frac{1}{1+\delta} \text{Re}\left((\tilde{\phi} - \tilde{V}_0) (\tilde{\mathbf{E}} - \tilde{\mathbf{E}} \cdot \mathbf{n} \cdot \mathbf{n})^*\right) \end{aligned} \quad (13)$$

Here the asterisk is the complex conjugate operator. The ICEO convective flow in sinusoidal steady state is then resolved by

inserting Eq.(13) into the Stokes equation as an effective boundary condition on the surface of the bipolar electrode, with all other surfaces being treated as no-slip wall boundaries. Although $|\zeta|$ exceeds 0.5V at low field frequencies, this bi-layer asymptotic model can manage to capture many qualitative features of ICEO flows at large voltages.

2.5 Physical process of ICEO in current microfluidic device

We then deal with the standard physical process of ICEK in the absence of possible Faradic current injection. Under the action of an initial normal field component on the metal surface, transient start-up of ionic electro-migration occurs with the motion of cations and anions being along and against the direction of the field, respectively (Figure 1(c)). After a characteristic RC charging time $\tau_{RC} = RC_d / \sigma_f (1 + \delta) = \varepsilon R / \sigma_f \lambda_D (1 + \delta)$ (Here R is the characteristic macroscopic length scale and equals 0.195L in the current problem), an ionic charge cloud of dipolar nature is formed on the polarizable metal (or any dielectric [16-18]) surface. This IDL has a thickness of typical Debye length $\lambda_D = \sqrt{D\varepsilon_f / \sigma_f}$ ($D = 2 \times 10^{-9} m^2/s$ is the ionic diffusivity), which lies in the range of 0.5nm~100nm in the context of aqueous solutions. At steady state, the non-uniform distribution of an induced surface charge in the Debye layer $-\tilde{q} = -C_0(\tilde{V}_0 - \tilde{\phi})$ fully repels the bulk field lines, which makes the conducting surface behave like an insulator. The tangential field component acting on the screening charge $-\tilde{q}$ gives rise to a pair of counter-rotating ICEO micro-vortices, resulting in a flow stagnation region at the center of the electrode surface that may be exploited for rapid particle trapping at appropriate conditions (Figure 1(d)). When the applied AC field frequency exceeds the surface-averaged RC charging frequency $f_{RC-average} = \sigma_f (1 + \delta) / 2\pi C_d (0.195L) = 210Hz$ for the equivalent circuit of the bulk resistance in series with the interfacial total capacitance, there is insufficient time for the induced charge to accumulate in the diffuse screening cloud due to a relaxation process. Consequently, the metal surface recovers to its intrinsic role of a perfect conductor above $f_{RC-average}$, and ICEO decreases by 50% at $f_{RC-average}$ (Figure 1(d)).

2.6 Dielectrophoresis

For getting observable ICEO, homogenous 1:1 binary symmetric KCl aqueous solutions of electrical conductivity $\sigma_f = 0.0008S/m$ are used in current experiment, yeast cells with approximate radius $r = 2.5\mu m$ in this suspending medium have a polarization factor $Re(f_{CM}(\omega))$ varying from 0.25 to 0.29 in the frequency range of interest, implying they suffer from a time-averaged positive dielectrophoretic (DEP) force in an AC field

$$\langle \mathbf{F}_{DEP} \rangle = \pi \varepsilon_f r^3 Re(f_{CM}(\omega)) \nabla (\tilde{\mathbf{E}} \cdot \tilde{\mathbf{E}}^*) \quad (14)$$

That attracts them to the electrode edge rather than its surface. It is noteworthy that both electric field phasor $\tilde{\mathbf{E}}$ and DEP force are frequency-dependent in the presence of double-layer polarization.

3 Materials and methods

3.1 Chip fabrication

Transparent thin-film indium tin oxid (ITO) is employed as the electrode material to give a clear view of movement of particles in the channel. Glass slides deposited with conducting ITO film (6.5-6.8Ω sheet resistance, 220±30nm thick ITO film, 80% in transmittance) are obtained from Kaivo Optoelectronic Technology (Zhuhai, Guangdong, China). An ITO-coated glass slide is washed with acetone and methanol for three times, rinsed with DI water, and dried at 100°C for 30min. Similar to the method used in Ref.[19], the slide is then laminated by negative dry film (Riston SD238, Dupont, USA). The slide is exposed to ultraviolet light (Figure 2(c)) and then developed in 0.85w% sodium carbonate solution for 5min, after which the slide is submerged in 9M HCl solution for 30 minutes to etch off the ITO in direct contact with the solvent. After etching, the remaining dry film resist is stripped off with acetone for 5 minutes.

We use PMMA pattern as mold to fabricate PDMS microchannel. A piece of PMMA sheet of 500μm in thickness is adhered to a clean glass slide using double-sided bonding tape. The PMMA sheet is then patterned using a laser cutter by following the CAD design of the microchannel pattern. PDMS microchannel is polymerized using the PMMA pattern as a mold. After stripped off, the PDMS slab and the glass slide with ITO electrode patterns are treated in an O₂ plasma cleaner (ZEPTO, Diener, Germany) for 32s (700mTorr chamber pressure, 20W RIE), and then the two components are aligned and bonded together under an optical microscope. Finally, the device is placed in an oven at 80°C for 1h to enhance the chemical bonding. The fabrication process is shown in Figure 2.

3.2 Sample preparation

To prepare yeast cells, 50mg of Baker's dry yeast is reactivated in 10mL DI water at 30°C for 1h. After reactivation, yeast suspension of 1mL is transferred to a centrifuge tube and washed three times. Then the yeast cells are transferred to 1mL of a 8 μS/cm KCl solution. Prior to each experiment, the prepared yeast solution is diluted 50 times using KCl solution with identical conductivity, and a 5% bovine serum albumin (BSA) solution is used to coat the microchannel for ~2 h to prevent adhesion of particles, then thoroughly washed with a KCl solution to remove BSA. A micrograph of viable yeast cells is shown in Fig.1(g).

3.3 Experimental setup

The AC sinusoidal voltages energized on the ITO electrodes are generated by a function generator (TGA12104, TTI, UK) in series with a signal amplifier (Model2350, TEGAM, USA), and monitored by an oscilloscope (TDS2024, Tektronix, USA). The motion of particles is observed under an optical microscope (BX53, Olympus, Japan) and recorded using a CCD camera (RETIGA2000R, Qimaging, Canada).

As shown in Figure 1(a) and Figure 4(a), a pair of coplanar ITO driving electrodes separated by a distance of G=3mm is

imposed with an AC voltage difference of $V_1(t) = A_1 \cos(\omega t + \theta)$, with field frequency $f = \omega/2\pi$ and amplitude A_1 varying in the range of 10Hz-10kHz and 12.5V-62.5V, respectively. One of the driving electrodes is grounded (Figure 4(a)). A floating

bipolar electrode of width $L=200\mu\text{m}$ is fixed in the gap center (Figure 1(a)(b)), and originally has a natural inducing potential $V_0(t) = A_1 \cos(\omega t + \theta)/2$.

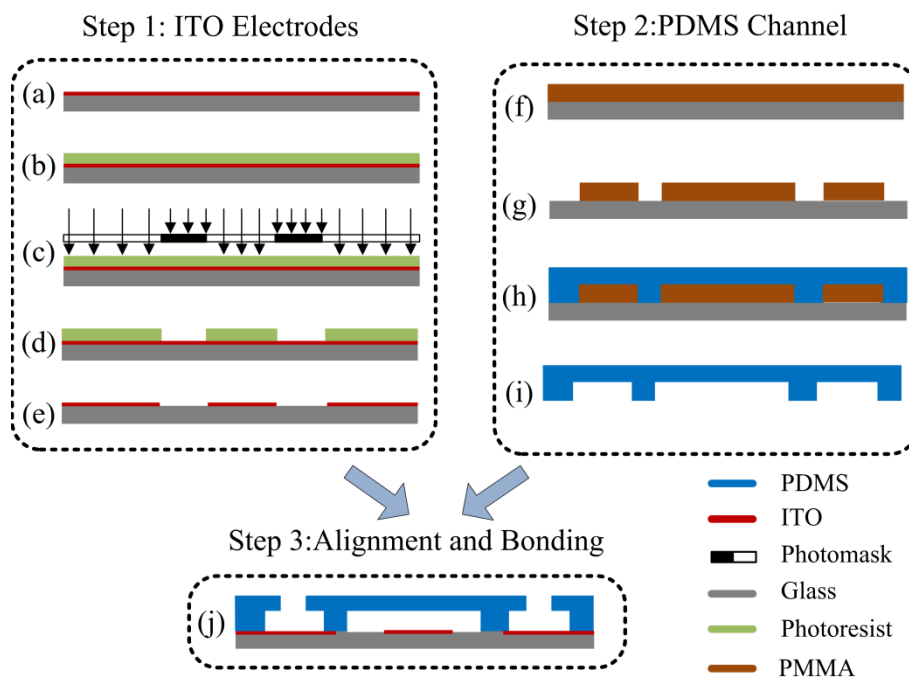


Figure 2 Fabrication process of the experimental chip: (a) Clean the ITO-coated glass slide; (b) Laminate negative dry film; (c) Ultraviolet light exposure; (d) Development; (e) ITO etching; (f) Adhere a PMMA sheet of $500\mu\text{m}$ thickness to a glass substrate; (g) Pattern the PMMA sheet by using a laser cutter; (h) Polymerize the PDMS microchannel using the PMMA pattern as a mold; (i) Strip off PDMS slab; (j) Alignment and bonding.

4. Results and discussion

4.1 Particle trapping on the surface of a floating electrode

Possibility of particle trapping around the central flow stagnation region (Figure 1(d)) by ICEO is at first tested below $f_{RC-average}$. When a low-frequency AC signal such as $f=10\text{Hz}$ is applied, no trapping occurs, and particles keep on moving in a constant rotation fashion independent of the voltage amplitude employed (SI.Movie), which is a good

indicator of flow velocity as particle DEP motion theoretically vanishes around a flat insulator (Figure 1(d)(e)).

At 200Hz and $A_1=37.5\text{V}$, particles from both sides move quickly to the central region due to the initial propulsion effect of ICEO fluidic drag and then aggregate to form a narrow linear pattern (Figure 3(a)). This transient collection is erratic, however, because these particles are at once carried away by the upward flow component and perform synchronous recirculation motion with ICEO fluid rolls (Figure 3(b)).

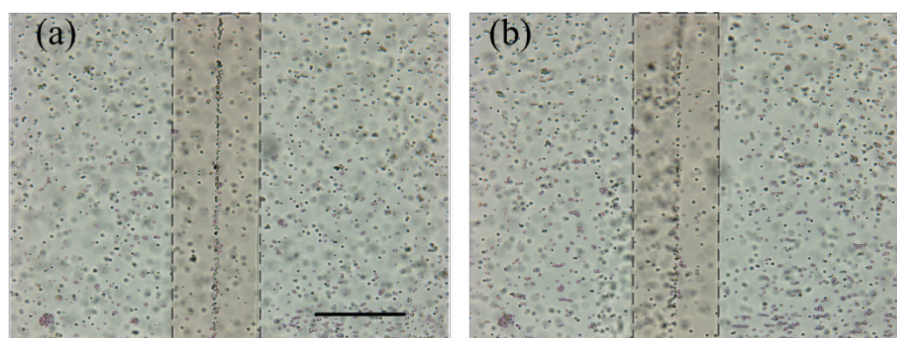


Figure 3 Erratic trapping behavior of yeast cells by ICEO under AC voltage at 200Hz and 37.5V on the surface of the floating electrode: (a) for $t=6.4\text{s}$ after turning on the AC power, particles aggregate to form a narrow linear pattern at the central region (scale bar $200\mu\text{m}$); (b) Unstable collection is demonstrated as the accumulation pattern becomes mutilated for $t=16\text{s}$.

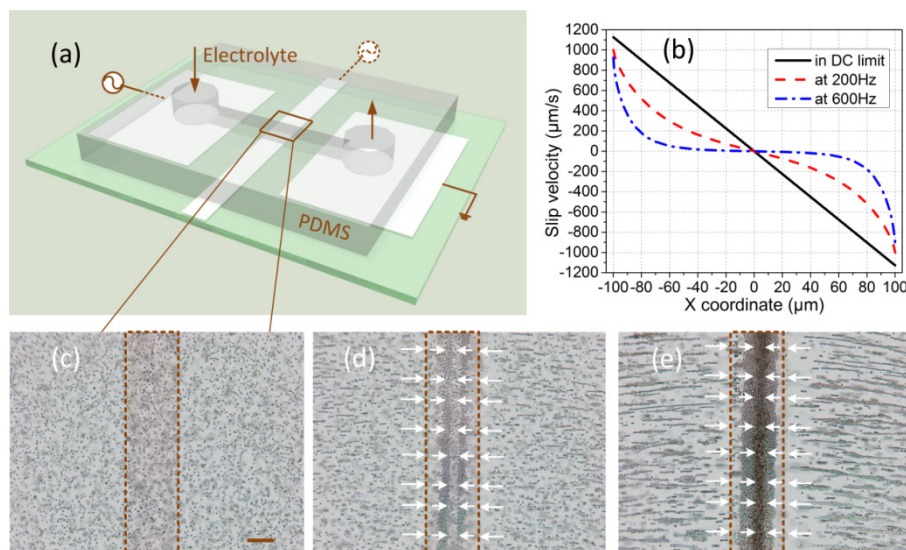


Figure 4 (a) A 3D schematic of our experiment chip. An ITO electrode of width $L=200\mu\text{m}$ is located at the center of a microchannel, and is either floating in potential or directly acting as a gate electrode. The ITO driving electrodes near electrolyte ports have an inter-electrode distance of $G=3\text{mm}$. (b) Time-averaged ICEO slip profiles on the surface of the bipolar electrode at different field frequencies from direct numerical simulation. (c)-(e) Stable concentration of yeast cells by ICEO under AC voltage at 600Hz and 62.5V: (c) for $t=0$, initial distribution of yeast cells without AC power (scale bar $100\mu\text{m}$); (d) for $t=12\text{s}$, particles rapidly pass the electrode rim at a tremendous speed to the central region; (e) for $t=108\text{s}$, steady trapping is proved by a widened accumulation pattern.

On increasing field frequency to 600Hz above a characteristic double-layer relaxation frequency $f_{RC-average}$, stable particle collection by ICEO occurs (Figure 4(c)-(e)). Switching on the power, most of the cells quickly move towards the electrode surface from both sides at a surprising speed (SI.Movie), but their velocity decreases rapidly in the immediate vicinity of electrode edge, which can be explained by the nonlinear slip

profile at 600Hz (Figure 4(b)). It is noteworthy that a few particles are trapped at the rim region by short-range positive DEP (pDEP) attraction, which helps attribute the physical mechanism of this long-range collection phenomenon to ICEO streaming flow rather than electrostatic force. Besides, stable trapping is evidenced by a widened concentration pattern from $t=12\text{s}$ (Figure 4(d)) to $t=108\text{s}$ (Figure 4(e)).

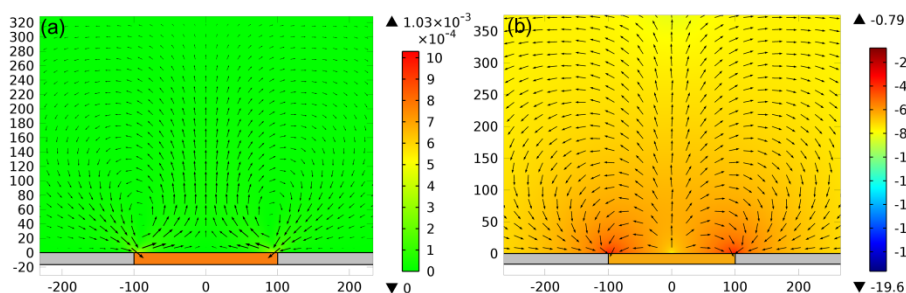


Figure 5 At $f=600\text{Hz}$ and $A_1=62.5\text{V}$, a surface and arrow plot of: (a) ICEO fluid flow (unit: m/s); (b) and pDEP velocity of yeast cells (unit: 10^4m/s) with the numbers on the margin of the figures denoting the local x- or y- coordinate.

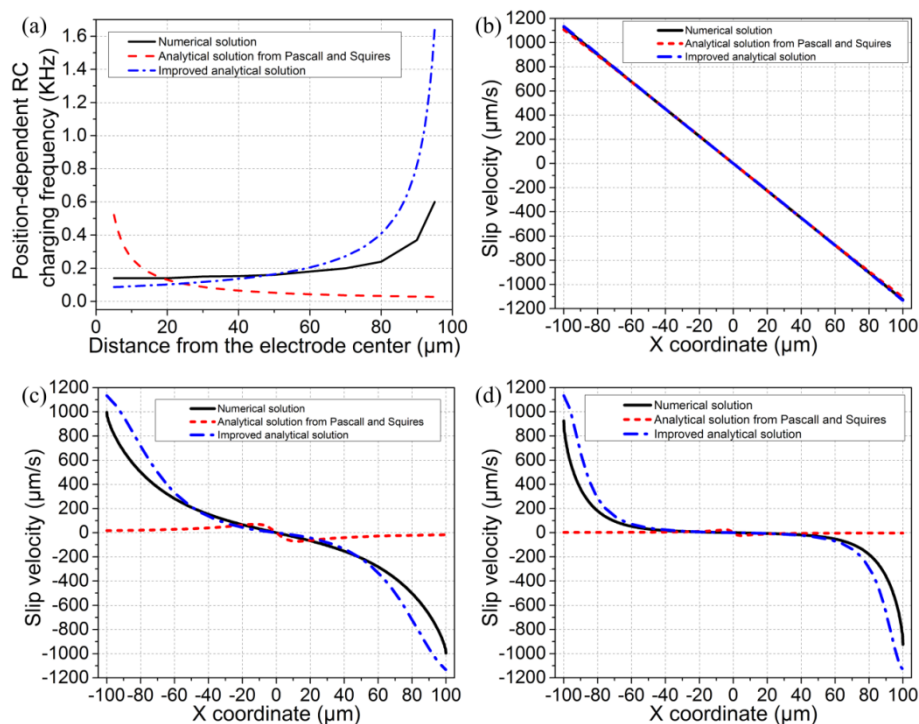


Figure 6 (a) Predictions of position-dependent RC charging frequency along the metal/electrolyte interface from different theoretical models. (b)-(c) A comparison among ICEO slip profiles on top of the bipolar electrode predicted by various theoretical models at different field frequencies: (b) in DC limit (4Hz); (c) around the RC charging frequency (210Hz); (d) at 600Hz.

A weak field region is created at the center of the conducting surface above the RC frequency, so that particle motion induced by pDEP force on the order of 10nm/s (Figure 5(b)), as calculated by grid-independent direct numerical simulation (DNS) using a commercial FEM software package (Comsol Multiphysics 4.4), points in the same direction as the upward ICEO fluidic drag (Figure 5(a)) near the stagnation region (F_{pDEP} and F_{ICEO} in Figure 1(f)), and is not a critical factor affecting particle trapping. Attention is then paid to the transversal ICEO slip on the electrode surface (Figure 4(b)). The linear slip profile in DC limit transits gradually to a nonlinear one above $f_{RC-average}$ at 600Hz due to inhomogeneous ionic charge relaxation along the metal/electrolyte interface (Figure 6(a)). At 600Hz, the fast fluid flow near the electrode edge can overcome the intense short-range pDEP attraction there, so as to make most of the particles entrained by long-range bulk ICEO vortical flows enter the electrode surface. Moreover, what ensues is that the abruptly weakened slip velocity at the central region contributes to trap large amounts

of those particles moving gently on top of the bipolar electrode by triggering a small upward ICEO flow component. Specifically, particle motion induced by the upward fluidic drag at the central region (F_{ICEO} in Figure 1(f)) is $0.829\mu\text{m/s}$ for yeast cells at 600Hz (for they stagnates approximately at the height of their radius, i.e. $y=r=2.5\mu\text{m}$) and is much smaller compared with $27.3\mu\text{m/s}$ in DC limit, which gives the downward buoyancy force $F_{buoyancy}$ a chance to dominate in the vertical direction at 600Hz. As a consequence, we can use such an elaborate nonlinear slip profile with large edge/inner and edge/upward flow velocity ratios above the double-layer relaxation frequency (Table 1 and Figure 1(b)) to effectively trap particles entrained by long-range bulk ICEO flows from two aspects: (i) A large driven force at the electrode edge is highly effective in transporting large amount of particles at a tremendous speed from the bulk fluid; (ii) Small upward ICEO flow component induced by weak transverse slip at the central part realizes stable particle trapping on the electrode surface.

Table 1 Calculation of frequency-dependent edge/inner and edge/upward flow velocity ratios by direct numerical simulation, with the positions of A1-A3 being indicated in Figure 1(b)

	Velocity magnitude at A1 (-90 μm , 0)	Velocity magnitude at A2 (-20 μm , 0)	Velocity magnitude at A3 (0, 2.5 μm)	Edge/inner velocity ratio A1/A2	Edge/upward velocity ratio A1/A3
4Hz	1000 $\mu\text{m/s}$	225 $\mu\text{m/s}$	27.3 $\mu\text{m/s}$	4.44	36.63
100Hz	876 $\mu\text{m/s}$	154 $\mu\text{m/s}$	18.6 $\mu\text{m/s}$	5.69	47.1
210Hz	676 $\mu\text{m/s}$	67 $\mu\text{m/s}$	8.07 $\mu\text{m/s}$	10.09	83.767
400Hz	480 $\mu\text{m/s}$	17.3 $\mu\text{m/s}$	2.14 $\mu\text{m/s}$	27.746	224.3
600Hz	362 $\mu\text{m/s}$	6.21 $\mu\text{m/s}$	0.829 $\mu\text{m/s}$	58.293	436.67

In order to better understand the none (10Hz)/erratic (200Hz)/stable (600Hz) particle trapping behaviors at different field frequencies, the analytical treatment for nonlinear

electrokinetic slip in a similar geometrical configuration from Pascall and Squires [15], as derived by making analogy with

AC electroosmotic phenomenon [20, 21], is concisely reviewed here:

$$\langle u_{slip} \rangle = \frac{-\varepsilon E^2 x}{2\mu(1+\delta)(1+\omega^2\tau_{c1}^2)} \quad (15)$$

where $\tau_{c1} = \pi|x|C_d/\sigma(1+\delta)$ and $f_{c1} = \sigma(1+\delta)/2\pi^2|x|C_d$ are the position-dependent RC charging time and frequency, respectively. The factor $(1+\delta)^{-1}$ accounts for the effect of an extra dielectric layer on the diffuse-charge dynamics, which has been incorporated into our bi-layer asymptotical model (Eq.(11) and Eq.(13)). f_{c1} predicts a lower relaxation frequency near the electrode edge due to a larger distance $|x|$ from the electrode centerline (Figure 6(a)). Consequently at a moderate frequency, the electrokinetic slip approaches zero at the electrode rim due to an earlier occurrence of ionic charge relaxation (Figure 6(c)), and simultaneously a higher relaxation frequency at the center of the electrode surface results in a quicker slip velocity there than that at the electrode edge at 600Hz (Figure 6(d)). As a consequence, though Eq.(15) can exactly predict fluid motion around the central region [15], it cannot explain the rapid particle motion across the electrode rim.

To rationalize this physical process, position-dependent RC charging frequency f_c along the metal/electrolyte interface is calculated by DNS. An increasing propensity of f_c with $|x|$ is observed ((Figure 6(a)), which encourages an improvement to Eq.(15):

$$\langle u_{slip} \rangle = \frac{-\varepsilon E^2 x}{2\mu(1+\delta)(1+\omega^2\tau_{c2}^2)} \quad (16)$$

where the charging characteristics become

$$\tau_{c2} = \left(\frac{L}{2} - |x|\right) C_d / \sigma(1+\delta) \quad \text{and}$$

$f_{c2} = \sigma(1+\delta)/2\pi\left(\frac{L}{2} - |x|\right)C_d$. f_{c2} predicts increasing RC charging frequency with $|x|$, in qualitative accordance with the result from DNS (Figure 6(a)). As shown in Figure 6(b), all the slip profiles predicted by the three physical models are not only linear but also in perfect coincidence in DC limit. In making the calculations, a prefactor 0.8 is introduced to both analytical treatments to account for the slight non-uniform field emission from the driving electrodes (Figure 1(a)). Both DNS and the improved analytical solution Eq.(16) can predict faster slip velocity near the electrode edge than that at the central part at 210Hz and 600Hz (Figure 6(c)(d)), due to the consideration of a lower ionic charge relaxation frequency around the stagnation region, which helps account for these frequency-dependent particle behaviors.

4.2 Position-controllable particle trapping by exploiting AC-FFET

Subsequently, with the concept of AC-FFET (refer to Appendix for a demonstration of this concept), we extend fixed-potential ICEO from DC to AC field to adjust the stagnation position of particles. The gate potential $V_0(t) = A_0 \cos(\omega t + \theta)$ of the original floating bipolar metal strip (gate electrode) is hereafter

externally energized by a function generator, and is completely in phase with the source potential $V_1(t) = A_1 \cos(\omega t + \theta)$ of the driving electrode. Since below the characteristic RC charging frequency electric field from the gate electrode (GE) is severely screened by induced ionic charge in IDL and thus GE becomes an insulator, surface potential outside the diffuse screening cloud cannot effectively redistribute due to the deviation of $V_0(t)$ from $V_1(t)/2$, which lays the foundation of Eq.(5.5) in Ref.[3]. In other words, in DC limit, applying a second AC signal $V_0(t)$ to the bipolar electrode different from its floating potential $V_1(t)/2$ means a direct control on the induced zeta potential without disturbing the surrounding field distribution. Consequently, a slight deviation of gate potential from its background value $V_1(t)/2$ would result in merely one dominating ICEO vortex without any stagnation line (Figure 7(b)), which violates the intention of particle trapping.

For ac field frequencies exceeding the reciprocal RC time scale, field from GE penetrates into the electrolyte bulk, such that immediate redistribution of surface potential occurs in response to a change in the applied gate potential, and broken symmetry of induced zeta potential and hence ICEO will take place if gate potential deviates from the natural inducing value. As a consequence, unlike previous researchers [1, 3], we prefer to take advantage of the phenomenon of AC-FFET above the characteristic RC relaxation frequency rather than in a steady DC field. The inset image of Figure 7(a) shows the experimental results of particle trapping by fixed-potential ICEO under the condition of $f=600\text{Hz}$, $A_1=62.5\text{V}$, $A_0=(23.75\text{V}, 27.5\text{V}, 31.25\text{V}, 35\text{V}, 38.75\text{V})$, respectively, corresponding to a normalized potential deviation $(A_0 - A_1/2)/(A_1/2)$ ranging from -0.24 to 0.24. Formation of particle assembly line at different positions is achieved by adjusting the potential amplitude A_0 imposed on GE.

AC-FFET above the RC charging frequency in this geometrical configuration is originated by left-right asymmetry in Ohmic current flowing into the Debye layer, since the bias voltage A_0 of the bipolar electrode can penetrate into the outside of IDL. When $A_0 < \frac{A_1}{2}$, field intensity in the left inter-electrode gap (Figure 4(a)) dominates over the right gap, which drives more intense double-layer charging on the left side of electrode surface according to Eq.(11) and hence makes the left ICEO vortex dominate over the right one (Figure 7(c)), resulting in a shift of particle trapping center ($x>0$) toward the right side of electrode surface (Figure 7(a)(b)); And vice versa (Figure 7(d)), i.e. $A_0 > \frac{A_1}{2}$ corresponds to a negative x- coordinate of particle trapping center ($x<0$).

Besides, experimental observation shows the distance of particle trapping center to the electrode centerline is approximately a linear function of potential deviation $(A_0 - A_1/2)$ at 600Hz (Figure 7(a)), which is in qualitative agreement with the simulation results (Figure 7(b)). This conclusion suggests applying sinusoidal voltages of amplitude A_0 deviating enough from the background value $A_1/2$ to capture particles at desired locations on the electrode surface.

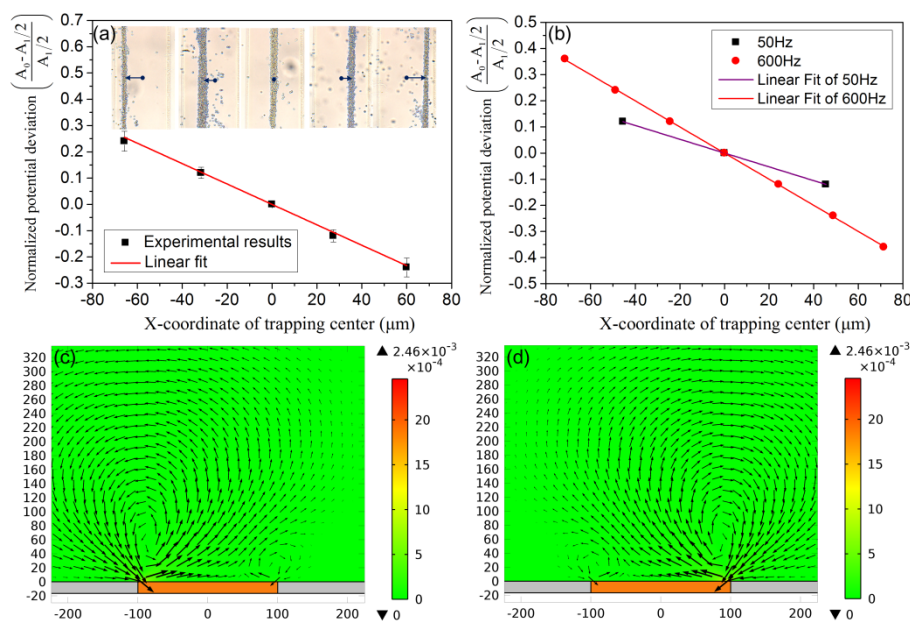


Figure 7 Controllable particle trapping by fixed-potential ICEO: (a) Distance of the center of particle assembly line to the electrode centerline as a function of potential deviation at 600Hz, with the inset showing assembly pattern on the electrode surface at different gate potential amplitude A_0 . The arrows indicate the directions of particle motion; (b) Prediction on the position of particle trapping center by DNS for different gate potential at 50Hz and 600Hz. There is no flow stagnation region at 50Hz if $|(A_0 - A_1/2)/(A_1/2)| > 0.12$. When $f=600\text{Hz}$ and $A_1=62.5\text{V}$ are fixed, a surface and arrow plot of ICEO flow for (c) $A_0=23.75\text{V}$; (d) $A_0=38.75\text{V}$

4.3 Potential impact of Joule medium heating on particle trapping

Non-uniform Joule medium heating above electrode surfaces can result in electrothermal flow (ETF) [22-24] and buoyancy flow (BF) [25] in the electrolyte bulk, both of which can affect particle trapping at a sufficient liquid conductivity in this microfluidic device where the interelectrode gap size reaches $\sim 1\text{mm}$. However, it is not suitable to use this fluidic device to trap particles by bulk electro-convection from ETF and BF at such a high price of surprise temperature elevation even if a high conductivity solution is used, because effective ETF induced by Joule heating is often produced above closely placed microelectrode array rather than this kind of geometrical configuration with interelectrode distance much larger than the electrode width (Figure 1(a)).

5. Conclusion

In summary, on the basis of ICEO, we develop a method of position-controllable particle trapping on the surface of a bipolar metal strip. Yeast cells are trapped at the central flow stagnation region above a characteristic RC charging frequency when the bipolar electrode is floating in potential, due to inhomogeneous ionic charge relaxation along the metal/electrolyte interface. By extending AC-FFET from DC limit to AC field, we find fixed-potential ICEO beyond the reciprocal RC time scale is more favorable in generating controllable symmetry breaking in vortex flow pattern than that in a steady DC field, resulting in position-controllable trapping of particles by adjusting the potential amplitude of GE. For AC-FFET, although the double-layer charging mechanism above the RC charging frequency is more complicated than that in DC

limit, both experimental observation and simulation results indicate that the distance of particle trapping center to the electrode centerline is still approximately a linear function of the potential deviation at 600Hz above $f_{RC-average}$. These results suggest that ICEO may be one powerful tool that contributes to particle sample manipulation in modern microfluidic systems.

Acknowledgements

We gratefully acknowledge the National Natural Science Foundation of China (No.51305106), the Fundamental Research Funds for the Central Universities (Grant No. HIT.NSRIF. 2014058 and Grant No. HIT. IBRSEM. 201319), and the Open Foundation of the State Key Laboratory of Fluid Power Transmission and Control (GZKF-201402).

Appendix

In fixed-potential ICEO, the potential of a polarizable object is controlled so as to induce total surface charge in the diffuse double-layer in phase with a (steady or oscillating) background field [1]. This effect is essentially an AC generalization of the “flow field effect transistor” [26,27], similar to the work of van der Wouden et al [28].

When the AC voltage imposed on the left electrode is $A_1 \cos(\omega t)$, the right electrode is grounded, and potential distribution just outside the double layer of the middle electrode is $\phi(t)$, we can derive an analytical solution of the induced zeta

potential ζ in DC limit (0Hz) to see whether the biased voltage has any effect on the induced surface charge

1. When the middle electrode is floating in potential

$$\begin{aligned}\zeta(t) &= \frac{1}{1+\delta} \left[\frac{A_1}{2} \cos(\omega t) - \phi(t) \right] \\ &= \frac{1}{1+\delta} \left[Ex \cos(\omega t) \right]\end{aligned}\quad \text{Eq.(A1)}$$

2. When the middle electrode acts as a gate electrode and hence has a fixed-potential $A_0 \cos(\omega t)$

$$\begin{aligned}\zeta(t) &= \frac{1}{1+\delta} \left[A_0 \cos(\omega t) - \phi(t) \right] \\ &= \frac{1}{1+\delta} \left[A_0 \cos(\omega t) - \frac{A_1}{2} \cos(\omega t) + \frac{A_1}{2} \cos(\omega t) - \phi(t) \right] \\ &= \frac{1}{1+\delta} \left[Ex \cos(\omega t) + \left(A_0 - \frac{A_1}{2} \right) \cos(\omega t) \right]\end{aligned}\quad \text{Eq.(A2)}$$

The induced surface charge density in the diffuse double-layer in DC limit is given by

$$q = C_d \zeta = \frac{C_d}{1+\delta} \left[Ex \cos(\omega t) + \left(A_0 - \frac{A_1}{2} \right) \cos(\omega t) \right] \quad \text{Eq.(A3)}$$

According to the Helmholtz-Smoluchowski formula, ICEO slip expression on the surface of gate electrode in DC limit is

$$\begin{aligned}\langle u_{slip} \rangle &= \frac{-\varepsilon \zeta E_t}{\mu} \\ &= \frac{-\varepsilon}{\mu} \left\langle \frac{1}{1+\delta} \left[Ex \cos(\omega t) + \left(A_0 - \frac{A_1}{2} \right) \cos(\omega t) \right] \cdot E \cos(\omega t) \right\rangle \\ &= \frac{-\varepsilon E}{2\mu(1+\delta)} \left(Ex + A_0 - \frac{A_1}{2} \right)\end{aligned}\quad \text{Eq.(A4)}$$

The x-coordinate of flow stagnation region is

$$x = (A_1/2 - A_0)/E \quad \text{Eq.(A5)}$$

In analogy with a field effect transistor (FET) where varying the gate voltage can adjust the output electric current, changing the amplitude of the gate voltage in this fluidic device can adjust the induced surface charge density in the diffuse double-layer so as to generate controllable symmetry breaking in ICEO vortex flow pattern Eq.(A5). As a result, it is reasonable that the biased voltage on the gate electrode is called the technique of AC-flow field effect transistor (AC-FFET). In our practical experiments, particles cannot be trapped on the electrode surface in DC limit due to a large upward ICEO flow component, so we raise the field frequency to achieve a successful trapping.

It is difficult to derive an analytical solution when the field frequency is raised above DC limit, however, since the electric field from the gate electrode penetrates outside the double-layer.

Instead, full numerical analysis is effective under this circumstance (Figure 7(b-d)).

Notes and references

^aSchool of Mechatronics Engineering, Harbin Institute of Technology, West Da-zhi Street 92, Harbin, Heilongjiang, P. R. China 150001

^bMicro and Nano-technology Research Center, State Key Laboratory for Manufacturing Systems Engineering, Xi'an Jiaotong University, Xianning Westroad 28, Xi'an, Shaanxi, P. R. China 710049

^cBoth authors contributed equally to this work.

^{*}Correspondence: Doctor Yukun Ren, Email: rykhit@hit.edu.cn

1 M. Z. Bazant and T. M. Squires, *Phys. Rev. Lett.*, 2004, **92**, 066101.

2 T. M. Squires and M. Z. Bazant, *J. Fluid Mech.*, 2004, **509**, 217.

3 T. M. Squires and M. Z. Bazant, *J. Fluid Mech.*, 2006, **65**, 560.

4 T. M. Squires and S. R. Quake, *Rev. Mod. Phys.*, 2005, **77**, 977.

5 C. K. Harnett, J. Templeton, K. A. Dunphy-Guzman, Y. M. Senousy, and M. P. Kanouff, *Lab Chip*, 2008, **8**, 565.

6 J. A. Levitan, S. Devasenathipathy, V. Studer, Y. X. Ben, T. Thorsen, T. M. Squires and M. Z. Bazant, *Colloid Surf. A*, 2005, **267**, 122.

7 K. A. Rose and J. G. Santiago, *Phys. Rev. E*, 2006, **75**, 197.

8 D. Saintillan, E. Darve and E. S. G. Shaqfeh, *J. Fluid Mech.*, 2006, **563**, 223.

9 M. S. Kilic and M. Z. Bazant, *Electrophoresis*, 2011, **32**, 614.

10 S. Gangwal, O. J. Cayre, M. Z. Bazant and O. D. Velev, *Phys. Rev. Lett.*, 2008, **100**, 058302.

11 Y. K. Ren, D. Morganti, H. Y. Jiang, A. Ramos and H. Morgan, *Langmuir*, 2011, **27**, 2128; P. García-Sánchez, Y. K. Ren, J. J. Arcenegui, H. Morgan and A. Ramos, *Langmuir*, 2012, **28**, 13861.

12 M. Z. Bazant, M. S. Kilic, B. D. Storey and A. Ajdari, *Adv. Colloid Interface Sci.*, 2009, **152**, 48.

13 S. M. Davidson, M. B. Andersen and A. Mani, *Phys. Rev. Lett.*, 2014, **112**, 128302.

14 S. J. Liu, H. H. Wei, S. H. Hwang and H. C. Chang, *Phys. Rev. E*, 2010, **82**, 026308.

15 A. J. Pascall and T. M. Squires, *Phys. Rev. Lett.*, 2010, **104**, 088301.

16 O. Schnitzer and E. Yariv, *Phys. Rev. E*, 2014, **89**, 043005.

17 Y. Eckstein, G. Yossifon, A. Seifert and T. Miloh, *J. Colloid Interface Sci.*, 2009, **338**, 243.

18 Z. Matan and G. Yossifon, *PHYS FLUIDS*, 2014, **26**, 082002.

19 N. A. M. Yunus and N. G. Green, *MICROSYST TECHNOL*, 2010, **16**, 2099.

20 A. Ramos, H. Morgan, N. G. Green and A. Castellanos, *J. Colloid Interface Sci.*, 1999, **217**, 420.

21 A. Ajdari, *Phys. Rev. E*, 2000, **61**, R45.

22 A. Kumar, J.S. Kwon, S. J. Williams, N. G. Green, N. K. Yip and S. T. Wereley, *Langmuir*, 2010, **26**, 5262.

23 V. Velasco and S. J. Williams, *J. Colloid Interface Sci.*, 2013, **394**, 598.

24 W. Y. Liu, Y. K. Ren, J. Y. Shao, H. Y. Jiang and Y. C. Ding, *J. Phys. D: Appl. Phys.*, 2014, **47**, 075501.

25 A. Castellanos, A. Ramos, A. Gonzalez, N. G. Green and H. Morgan, *J. Phys. D: Appl. Phys.*, 2003, **36**, 2584.

26 R. B. M. Schasfoort, S. Schlautmann, J. Hendrikse and A. van den Berg, *Science*, 1999, **286**, 942.

27 E.J. van der Wouden, T. Heuser, R.E. Oosterbroek, D.C. Hermes, J.G.E. Gardeniers and A. van den Berg, *COLLOID SURFACE A*, 2005, **267**, 110

28 E. J. van der Wouden, D. C. Hermes, J. G. E. Gardeniers, and A. van den Berg, *Lab on a Chip*, 2006, **6**, 1300.